Modelling of plasma current neutralization in the near plume of a Hall thruster via a 2D hybrid code

A. Domínguez-Vázquez*[1], J. Zhou[2], Alejandro Sevillano-González[2], E. Ahedo[2]

[1]Universidad de Málaga, 29071 Campanillas, Spain
[2]Universidad Carlos III de Madrid, 28911 Leganés, Spain

August 26, 2024

Abstract

Effects of plume truncation and cathode location on current neutralization in the plume of a Hall effect thruster are analyzed with a hybrid particle-in-cell/fluid code. A new global downstream matching layer (GDML) model that summarizes the plasma expansion to infinity is presented and compared to the common local null current condition. The GDML model ensures a globally current-free plume, provides expressions for the electron particle and energy fluxes at the quasineutral boundary of the truncated plume and estimates the final potential in the plume. Compared to the local null current condition, the GDML model significantly limits the influence of the plume boundary providing more robust results against the plume size for the longitudinal electron and electric current maps, especially when the external cathode is located outside the magnetic separatrix. Therefore, it increases the reliability of the simulation results obtained for smaller, less computationally demanding plume domains. While the ion expansion and the main thruster performance figures are practically unaffected by the plume size and the electron outflow conditions, the solution for the longitudinal electron currents provided by the GDML model is more representative of the still significantly magnetized electron population in the near plume region of a Hall thruster.

1   Introduction

In the near plume of a Hall effect thruster (HET) take place physically complex processes that remain not fully understood, and which play a central role in thruster unit performance and its integration with other spacecraft systems. In particular, current neutralization of the expanding plasma jet and the coupling between the ion beam and the electron flow emitted from the neutralizer cathode, are known to be affected by many factors, including the position of the cathode [1–7], its location relative to the magnetic configuration [8–12] and the electrical configuration of testing facilities [13–16]. Therefore, advances towards an accurate and predictive model of these processes in the near plume region of a HET are of central importance.

Many hybrid particle-in-cell (PIC)/fluid [17–23] and multi-fluid [24–26] HET simulation models used in HET research typically simulate the plasma discharge inside the thruster channel and in the near plume region, which is unavoidably truncated to limit computational effort. Boundary conditions reproducing faithfully the expansion to infinity of a current-free plasma jet must then be imposed at the downstream end of the truncated plume.

The simple null local current condition, which can be assumed valid for a sufficiently large plume only, is commonly used [19, 22, 24]. Authors in Ref. 27 noted that H6 thruster multi-fluid simulations required to place the downstream boundary at a distance of at least 10 channel lengths downstream the thruster exit plane to avoid artificially increased electron transport across magnetic lines due to the zero local current condition. Moreover, this boundary condition gives no information about the final potential in the plume nor

the electron energy flux through the plume boundary. Previous numerical studies with multi-fluid [24, 28] and hybrid [29] models have set the electron temperature at the plume boundary. In Ref. 28 it is found that the temperature solution in the near field (from about three channel lengths downstream the thruster exit) is largely driven by the prescribed boundary value, which is informed from plasma measurements. Therefore, this approach requires accurate electron temperature measurements in the plume, which may be only available for a limited range of operational conditions.

The goal of this paper is to present a model for the off-simulation region, including the electron dynamics, that attempts to reproduce faithfully the plasma expansion to infinity, where a final electric potential is reached in the globally current-free plasma plume, and provide appropriate boundary conditions in terms of electron particle and energy fluxes at the boundary of the truncated plume simulated by hybrid and multi-fluid HET models. Previous kinetic studies for both magnetized [30] and unmagnetized [31,32] plume expansions, have found that relevant features of the dynamics of the expansion are comparable to those of a Debye sheath. Based on the analogy, a global downstream matching layer (GDML) model is defined as a thin boundary layer relating relevant electron magnitudes at the quasineutral downstream plume boundary of the finite simulation domain and the infinity. The model permits to estimate a plume final potential at infinity assuring a globally current-free plasma plume, while locally decouples ion and electron currents at the plume boundary of the finite domain, and provides expressions for the electron particle and energy fluxes at the quasineutral plume boundary.

The performance of the GDML is evaluated and compared against the local null current condition through numerical simulations of a 5kW-class HET

---

*Corresponding author email: adoming@uma.es

with a conventional magnetic topology and an external cathode conducted with our 2D axisymmetric hybrid code HYPHEN [22, 33, 34]. First, placing the external cathode within the region enclosed by the magnetic separatrix in the near plume, results are compared for four different plume sizes. Second, the radial position of the cathode is increased to locate it outside the magnetic separatrix. In this scenario, current neutralization in the near plume is expected to be more affected by the boundary of the truncated plume, since the pathways of a large fraction of magnetized cathode-born electrons correspond to field lines intersecting the downstream plume boundary.

The rest of the paper is organized as follows. Sec. 2 presents the GDML model and its implementation within HYPHEN. Secs. 3 and 4 compare the simulation results obtained with both the null local current condition and the GDML model for different plume sizes and cathode positions. Finally, Sec. 5 summarizes the conclusions.

2 Simulation model

2.1 Generalities

A 5 kW-class HET with a conventional (non-shielded) magnetic topology is considered in this study. Figs. 1(a)-(b) sketches the simulation domain, which comprises the thruster annular vessel (with length $L_c = 29$ mm, width $H_c = 22.2$ mm and inner radius 54.5 mm), and the near plume region. Fig. 1(c) shows the applied magnetic field $\boldsymbol{B}$ magnitude map and streamlines. Corresponding magnetic lines are represented by the blue lines in Fig. 1(b), including the (off-axis) magnetic separatrix in the near plume passing through the magnetic singular point located at the axis at $z/L_c = 6.2$. The peak of $B \equiv |\boldsymbol{B}|$ along the thruster channel midline is 245.06 G, at $z/L_c = 0.86$. The thruster anode corresponds to the complete channel back wall and the cathode is located off-axis at the thruster exit plane, [refer to Fig. 1(b)]. A power source sets the discharge voltage V_d between anode and cathode. The reference of the electric potential ϕ is set at the cathode, so that the potential of the anode wall is V_d. The total xenon neutral mass flow rate injected into the domain is $\dot{m} = \dot{m}_A + \dot{m}_C$, where $\dot{m}_A$ and $\dot{m}_C$ are the mass flow rates injected through the anode and the cathode, respectively. The discharge current I_d collected at the anode wall provides the electron flow injected at the cathode.

The plasma discharge in thruster and the near plume region is simulated with the axisymmetric hybrid code HYPHEN, whose characteristics have been detailed in previous works [22, 33, 35, 36] and are briefly outlined next. HYPHEN is composed of three main modules coupled within a time-marching sequential loop. The ion (I)-module operates on a structured (PIC) mesh of the simulation domain [refer to Fig. 1(a)] and implements a PIC method to solve the dy-
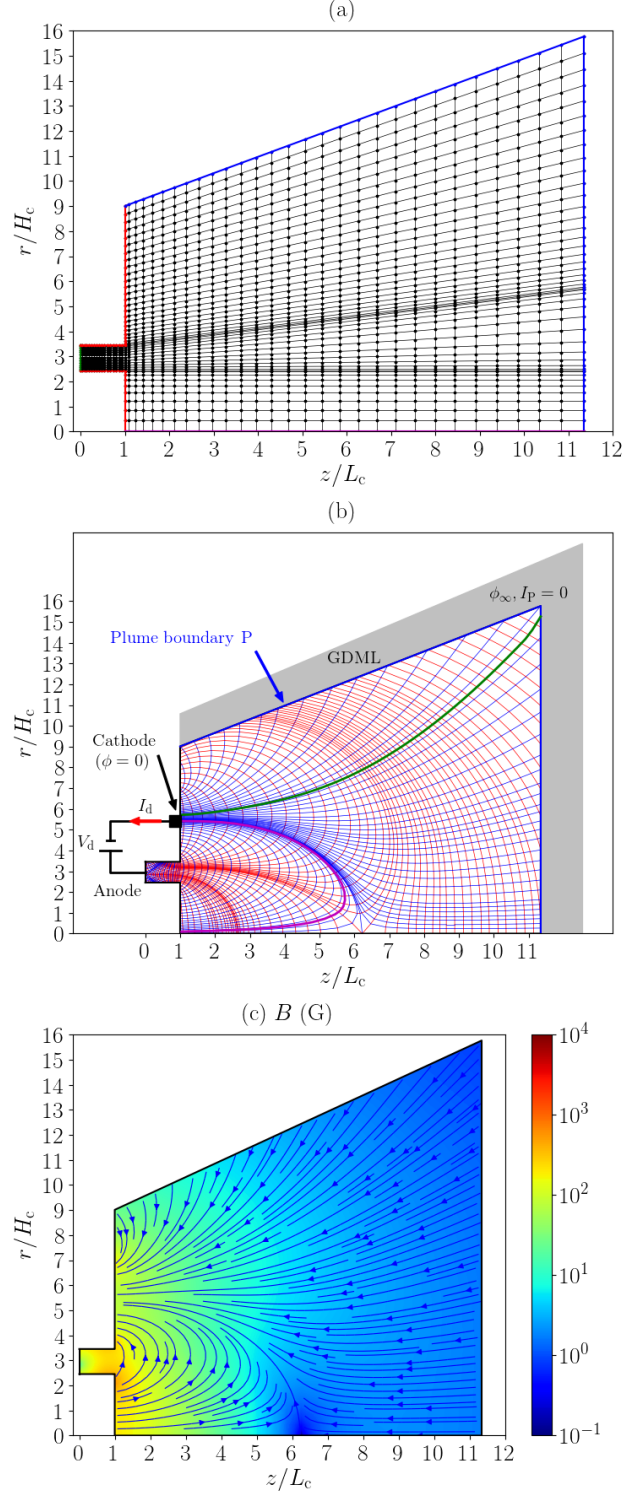

Figure 1: (a) The PIC mesh used by the I-module. The red, green, blue and magenta lines indicate the thruster dielectric walls, the anode wall, the plume boundary P, and the symmetry axis, respectively. (b) The MFAM used by the E-module. Inner blue and red lines are B-parallel and B-perpendicular lines, respectively, defining the cells. The magenta and green lines correspond to the cathode magnetic lines when the cathode is placed inside and outside the magnetic separatrix. (c) 2D (z, r) map of $B \equiv |\boldsymbol{B}|$ and magnetic streamlines. All figures correspond to plume size P3.

namics of the heavy species (i.e. ions and neutrals) obtaining the plasma density n_e and the net ion cur-

rent density vector $\boldsymbol{j}_i$. The electron (E)-module solves a quasineutral drift-diffusion fluid model for the magnetized electron population on an unstructured magnetic field align mesh (MFAM) [37], obtained from $\boldsymbol{B}$ and shown in Fig. 1(b), where red lines correspond to magnetic equipotential lines. It provides the solution for ϕ and the electron temperature T_e, current density vector $\boldsymbol{j}_e$ and energy flux vector $\boldsymbol{P}''_e = 5n_e T_e \boldsymbol{u}_e/2 + \boldsymbol{q}_e$ (sum of enthalpy and heat fluxes). Therefore, the electric current density vector $\boldsymbol{j} = \boldsymbol{j}_e + \boldsymbol{j}_i$ is obtained. Interpolation between the PIC mesh and the MFAM is required for some plasma properties. An empirical model for the electron anomalous transport sets a turbulent electron collisionality proportional to the electron cyclotron frequency through a tuning function $\alpha_t(z, r)$ representing the electron local turbulence level (further details can be found in Ref. 22). Non-neutral effects are limited to thin, planar Debye sheaths, which are treated as electrostatic discontinuities around the thruster walls, and solved by the sheath (S)-module to provide the appropriate boundary conditions in terms of the wall-collected electron current $j_{ne} = \boldsymbol{1}_n \cdot \boldsymbol{j}_e$ and energy flux $P''_{ne} = \boldsymbol{1}_n \cdot \boldsymbol{P}''_e$ at each (quasineutral) MFAM boundary face, with $\boldsymbol{1}_n$ being the *outward* unit normal vector. Details on the implementation for dielectric and conducting walls (e.g. the anode wall at known potential V_d) can be found in Ref. 22 and are omitted here.

2.2 Conditions at the plume boundaries

The blue line in Fig. 1(b) shows the (quasineutral) plume boundary P. The common local null current condition at P

$$j_{neP} = -j_{niP}, \qquad (1)$$

is only justified for sufficiently large plumes, and gives no information about the value of final electric potential far downstream in the plume ϕ_∞ nor the electron energy flux leaving the finite domain. When Eq. (1) is imposed in HYPHEN, the electron energy flux at a given MFAM boundary face at P is set to

$$P''_{neP} = -cT_{eP}j_{neP}/e, \qquad (2)$$

with $c > 0$ a given constant parameter. Writing this energy flux as the sum of the enthalpy and heat fluxes permits to obtain the electron heat flux at P

$$q_{neP} = -c_q T_{eP} j_{neP}/e, \qquad (3)$$

where $c_q = c - 5/2$. Previous HYPHEN simulations of an electrodeless plasma thruster scenario with a magnetic nozzle for plasma acceleration in the plume used values of $c = 5/2$, $9/2$ and $13/2$, corresponding to $c_q = 0$, 2 and 4, respectively [36]. This work revealed a significant impact of c on the electron temperature solution for truncated plume domains, $c = 9/2$ yielding a better agreement among the results for two different

plume domain sizes. Here, we set $c = 9/2$ when the local null current condition is applied at P.

A new GDML model for the off-simulation region, summarizing the electron dynamics in the infinite plume expansion, is proposed here. The GDML is defined as a thin boundary layer providing the jump conditions for relevant electron magnitudes between P and the infinity, as sketched in Fig. 1(b). A first version of the GDML (partially similar to a classical Debye sheath) permits to obtain the infinity-to-cathode bias ϕ_∞ by imposing a global zero current condition at P

$$I_P = I_{eP} + I_{iP} = \int_P (j_{ne}(\phi_{\infty P}) + j_{ni})dS = 0, \qquad (4)$$

where the surface integral is performed over P, I_{eP} and I_{iP} are the total electron and ion currents collected at P, respectively, and j_{niP} is provided by the I-module. Assuming a thin, planar, unmagnetized, collisionless layer connecting P to infinity, a kinetic model for Maxwellian electrons provides

$$j_{ne}(\phi_{\infty P}) = -e\frac{n_{eP}\bar{c}_{eP}}{4}\exp\left(\frac{-e\phi_{\infty P}}{T_{eP}}\right), \qquad (5)$$

where $\bar{c}_{eP} = \sqrt{8T_{eP}/(\pi m_e)}$ and $\phi_{\infty P} = \phi_P - \phi_\infty$ is the local P-to-infinity potential fall, with ϕ_P the local potential at the quasineutral boundary face (with respect to cathode). The determination of j_{neP} requires to obtain first $\phi_{\infty P}$. At each boundary face of P, the nonlinear function $j_{neP}(\phi_{\infty P})$ in Eq. (5) is linearized and combined with a generalized Ohm's law for the electron current density (in the inertialess limit) yielding an equation for $\phi_P = \phi_\infty + \phi_{\infty P}$. Iterations on $\phi_{\infty P}$ are performed if required to obtain the value of ϕ_P that ensures current continuity at each boundary face. These equations at the P boundary faces are solved along with Eq. (4) for ϕ_∞, where the linearization of Eq. (5) is included. The GDML model locally decouples the local ion and electron currents collected at each P boundary face, so that they can collect a non-zero electric current (i.e. $j_{nP} = j_{neP}(\phi_{\infty P}) + j_{niP} \neq 0$).

The kinetic model provides expressions for the electron energy fluxes at infinity and at P:

$$P''_{ne\infty} = -2T_{eP}j_{neP}/e, \qquad (6)$$

$$P''_{neP} = P''_{ne\infty} - j_{neP}\phi_{\infty P}. \qquad (7)$$

Writing P''_{neP} in Eq. (7) in terms of the enthalpy and heat fluxes permits to obtain the electron heat flux at P

$$q_{neP} = P''_{neP} + \frac{5}{2}T_{eP}j_{neP}/e. \qquad (8)$$

2.3 Simulation cases

Four different plume domains (P1 to P4) are considered, featuring an axial extension of 100, 200, 300 and 400 mm ($3.4L_c$, $6.9L_c$, $10.3L_c$ and $13.8L_c$). For all cases, the plume domain extends radially up to 200

Simulation parameter	Units	Value
I-module mesh smallest grid size	mm	1
I-module mesh number of cells	-	969, 1284, 1509, 1734
I-module mesh number of nodes	-	1049, 1371, 1601, 2831
MFAM number of cells	-	1948, 2397, 3506, 4081
MFAM number of faces	-	4025, 4933, 7186, 8353
MFAM average cells skewness	(10^{-2}) -	7.06, 6.45, 5.49, 5.31
Ion-moving timestep, Δt	ns	15

Table 1: Main simulation parameters and mesh characteristics (values separated by commas refer to cases P1 to P4).

Case	F (mN)	F_i (mN)	F_e (mN)	F_n (mN)	V_{cc}	ϕ_∞
P1L	282.60	274.77	6.83	1.00	20.50	N/A
P2L	287.16	282.80	3.41	0.94	9.21	N/A
P3L	286.50	283.54	2.13	0.97	9.72	N/A
P4L	288.17	285.84	1.30	1.02	11.07	N/A
P2LC	268.62	260.10	7.67	0.84	51.71	N/A
P3LC	269.93	263.99	5.09	0.85	32.72	N/A
P1G	284.94	279.25	4.65	1.04	16.43	0.82
P2G	284.78	280.95	2.86	0.97	9.00	-0.70
P3G	285.35	282.44	1.93	0.98	9.06	-2.85
P4G	287.14	284.89	1.23	1.02	10.46	-2.82
P2GC	271.11	264.26	5.97	0.88	44.36	-7.14
P3GC	270.32	265.31	4.11	0.90	28.45	-12.68

Table 2: Thrust F and its contributions, coupling voltage V_{cc} and infinity-to-cathode potential ϕ_∞.

mm at the thruster exit plane (see Fig. 1). The radial extension of the downstream end increases with the plume length and is set to 250, 300, 350 and 400 mm for P1 to P4 cases, respectively, so that the PIC mesh approximately follows the ion beam expansion in the plume to limit particle depletion. For case P3, Figs. 1(a) and (b) show the PIC mesh and the MFAM, respectively. The average B value at the plume boundary P for cases P1 to P4 is 10.53, 5.81, 4.67 and 3.93 G, respectively. The main characteristics of the simulation domain meshes for cases P1 to P4 and the simulation timestep are listed in Tab. 1. Compared to P4 cases, simulations for P1, P2 and P3 cases are around 69%, 30% and 8% faster in a single core run.

Two cathode radial positions will be considered: a reference one at 120 mm, located within the region enclosed by the magnetic separatrix, whose magnetic line is represented by the magenta line in Fig. 1(b), and a more external location at 126.6 mm, outside the magnetic separatrix, whose magnetic line, depicted in green in Fig. 1(b), intersects the downstream axial boundary below the top right corner of the plume domain. For plume size P1, the axial downstream boundary of the plume intersects the cathode magnetic line, and the magnetic singular point is left outside the plume domain.

For the reference cathode position, Sec. 3 presents results for the four plume sizes P1 to P4 when either the local (L) zero net current condition or the GDML (G) model is applied at the plume boundary P. These eight simulation cases shall be referred to as PiL and PiG, with $i = 1, 2, 3, 4$. Sec. 4 analyzes the results for the off-reference cathode location in plumes P2 and P3. The four simulation cases are referred to as PiLC and PiGC, with $i = 2, 3$.

All simulation cases in this work consider a single thruster operating point with $V_d = 300$ V and xenon neutral mass flows $\dot{m}_A = 17.59$ mg/s and $\dot{m}_C = 1.32$ mg/s (details on neutral injection conditions can be found in Ref. [22]). Electron turbulence level is assumed independent of the plume size and boundary conditions applied in this study. Therefore, for all cases simulated, the same axial "step-out" profile for the turbulence level function α_t, with only two calibration parameters α_{t1} and α_{t2}, is considered. The transition point from α_{t1} to α_{t2} is located downstream the B peak, at $z/L_c = 1.49$. Values of $\alpha_{t1} = 1.2\%$ and $\alpha_{t2} = 4.8\%$ are fitted to reproduce prescribed values

for I_d and thrust, F.

3 GDML assessment for several plume sizes

3.1 Main performance figures and 1D axial plasma profiles in the near plume

The total thrust is obtained as

$$F = F_i + F_e + F_n \tag{9}$$

where F_i, F_e and F_n correspond to the contributions of ion, electron and neutral species (including CEX populations). Tab. 2 lists these quantities for all cases. Small variations (around 2% maximum) are found on F among cases, and the different contributions show the expected behavior: F_i is the dominant contribution, and exhibits a slight monotonic increase for larger plume domains; F_e maximum contribution to thrust amounts to around 2% only, and decreases with plume size; the neutral contribution is marginal ($\sim 0.3\%$).

Ion current and plasma power balances, along with related partial efficiencies, are defined in Appendix A. Similar average values of $I_d \approx 18$ A, total power deposited into the discharge $P \approx 5.5$ kW and thrust efficiency $\eta = F^2/(2\dot{m}P) \approx 40\%$ are obtained for all cases, with small changes ($<$1-2%) on partial contributions to balances and efficiencies (see Tabs. A.1 and A.2).

To clarify this behavior, axial profiles of ϕ, T_e, and n_e in the plume are analyzed next. Fig. 2 shows the results along the thruster channel midline for $z/L_c \geqslant 3$ for cases P1L-P4L (left column) and cases P1G-P4G (right column). The crossing point between the channel midline and the cathode magnetic line [refer to the magenta line in Fig. 1(b)] is located at $z/L_c = 5.4$ and indicated by the vertical black dot-dashed lines. All simulation cases present very similar profiles for $z/L_c < 3$ for all magnitudes (not shown), with peak values $T_e \approx 28$ eV and $n_e \approx 1.7 \cdot 10^{18}$ m^{-3}. Plume size
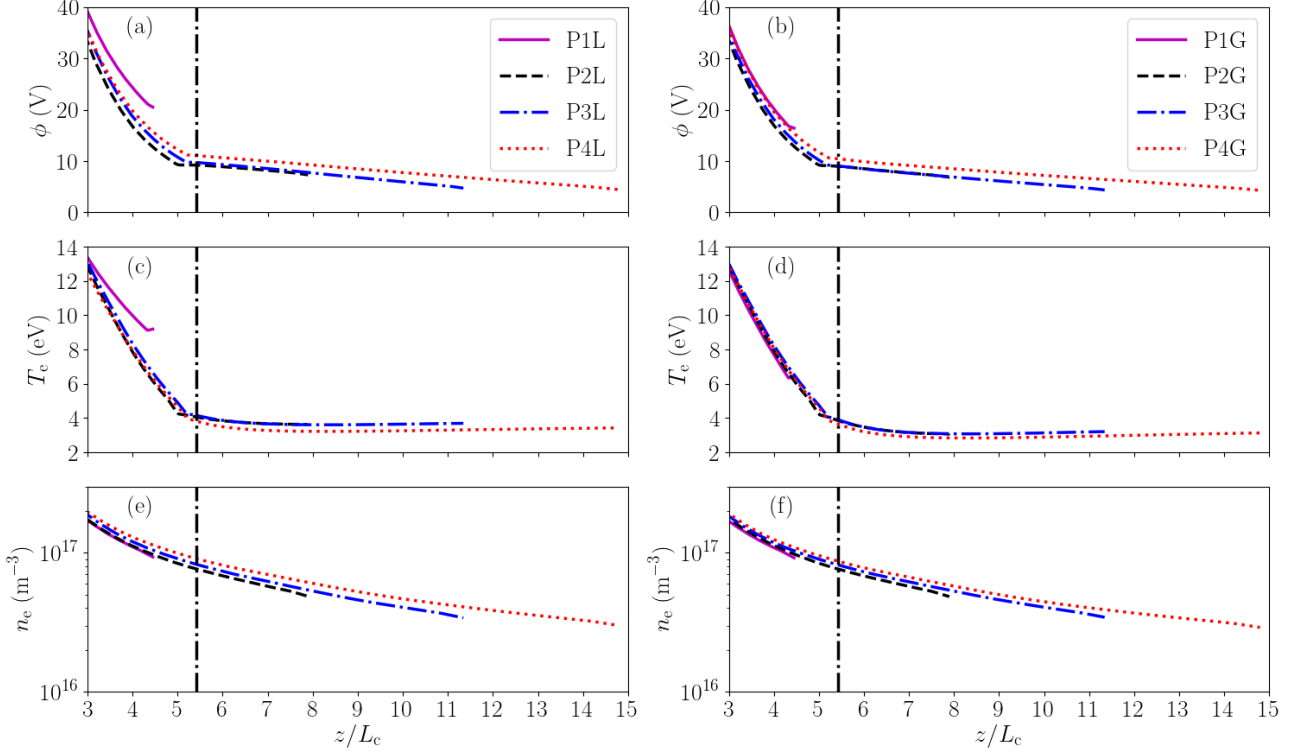
Figure 2: Time-averaged 1D axial profiles along the thruster channel midline in the near plume region for cases P1L-P4L (left column) and cases P1G-P4G (right column). (a)-(b) ϕ, (c)-(d) T_e and (e)-(f) n_e. The vertical black dot-dashed line indicates the crossing point with the cathode magnetic line at $z/L_c = 5.4$.

and electron boundary conditions at P induce moderate relative changes in the plume for these magnitudes, which are mild compared to the complete solution including the channel. The largest effects are observed on P1 cases, for which the cathode magnetic line is not fully contained within the simulation domain and crosses the P boundary. In particular, P1L case exhibits the maximum deviations on ϕ and T_e, being of about 3% of V_d and 10% of the T_e peak, respectively.

For cases P2-P4, the cathode coupling voltage V_{cc} is estimated as the electric potential value at the crossing point with the cathode magnetic line [38]. On the other hand, for P1 cases, V_{cc} values correspond to the electric potential of the final point of the axial profiles. Values for P1 and P3 cases are listed in Tab. 2. Maximum differences in V_{cc} among cases P2-P4 range around 0.5% of V_d only. This is consistent with the similar thrust values found for these cases (maximum difference among cases is of about 0.8%). Plume truncation in P1 cases induce higher V_{cc} values, indicating weaker cathode-coupling, in line with the lower F value obtained in these cases. Compared to P1L, the GDML model limits plume size effects in case P1G over V_{cc} and F.

P1L case yields hotter electrons in the plume, the final point of the axial profile (i.e. at P boundary) yielding $T_{eP}=9.38$ eV. On the other hand, T_e solution in case P1G is closer to that of larger plumes, with $T_{eP}=6.61$ eV. For P2-P4 cases, T_e remains nearly constant at relatively low values around 3 eV downstream

the cathode magnetic line (for $z/L_c > 5.4$), and no significant electron cooling is observed, in line with results in Ref. 28. Therefore, the electron thrust decrease with plume size is due to that of the plasma density at P.

Values of ϕ_∞ are listed in Tab. 2, ranging about 0.2-1.0% of V_d, suggesting a rather minor effect on the ion expansion downstream the simulated plume region. While a positive ϕ_∞ is obtained in case P1G, negative values are found for P2G-P4G cases. In the first case, the plume truncation hinders the ion beam neutralization, and a positive (with respect to cathode) ϕ_∞ develops to extract electrons from the cathode. For larger plume domains, the globally current-free plume at infinity imposes a negative with respect to cathode (i.e. electron confining) ϕ_∞ to regulate the electron flux leaving the domain.

3.2 Effect on 2D plasma current maps

Fig. 3 shows the 2D maps of magnitude of the longitudinal (i.e. axial-radial) electric current density $\tilde{\jmath} = \tilde{\jmath}_e + \tilde{\jmath}_i$ along with its corresponding streamlines for cases P1L-P4L (left column) and P1G-P4G (right column). The results for the ion longitudinal current density $\tilde{\jmath}_i$ show no significant differences among simulated cases and have been omitted for simplicity. For all cases, differences in $\tilde{\jmath}$ solution are due to changes in the electron longitudinal current density $\tilde{\jmath}_e$, as discussed later.

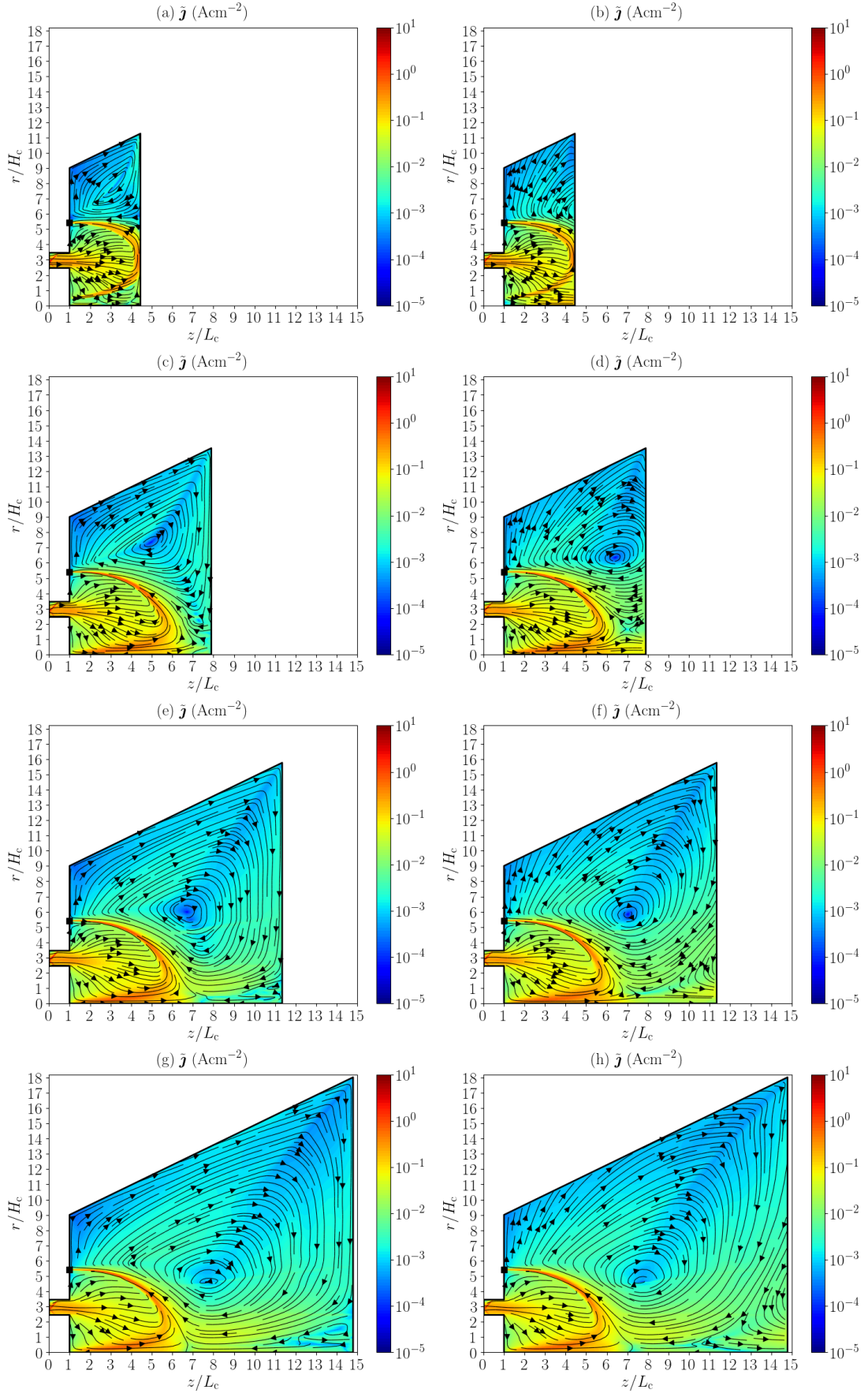Similar anode-to-cathode current loops are found

Figure 3: Time-averaged 2D (z,r) contour maps and streamlines of $\tilde{\boldsymbol{\jmath}}$ for P1L-P4L cases (left column) and P1G-P4G cases (right column). The black square marker indicates the cathode location.

for all cases (the channel lateral walls are dielectric, so that ion flows are canceled by electron ones yielding null local collected electric current). The electron boundary condition at P affects mainly the neutralization of the ion beam current in the region downstream the cathode magnetic line. The solution for $\tilde{\jmath}$ in this region is significantly more affected by the plume size in L cases, in which the local null current condition at P in Eq. (1) imposes $\tilde{\jmath}$ streamlines to be parallel to P, thus forcing the development of a current loop fully contained within the plume domain. On the other hand, the GDML model locally decouples the local ion and electron currents collected at P permitting a local non-zero electric current there. Along P, the electric current locally leaves the domain where the ion current dominates over the electron one, mainly near the symmetry axis and along the lateral plume boundary, and flows into the domain along a central part of the axial plume boundary, assuring $I_P = 0$, as stated in Eq. (4).

As expected, a similar $\tilde{\jmath}$ solution in the bulk plume domain is obtained in P4 cases, indicating that the local null current condition is only a good approximation for sufficiently large plume simulation domains. In both P4L and P4G cases, the null electric current point ($\tilde{\jmath} = \mathbf{0}$) in the bulk plume domain downstream the cathode magnetic line is located at $(z/L_c, r/H_c) \approx (7.7, 4.6)$. A larger variation of the location of this point is found for L cases compared to G cases. For P2L, it is located at $(z/L_c, r/H_c) \approx (5.0, 7.3)$, thus yielding a 35% and 59% axial and radial change, respectively, when compared to P4 cases. On the other hand, for case P2G we find a 17% and 28% axial and radial change, respectively, yielding $(z/L_c, r/H_c) \approx (6.4, 6.4)$.

The largest discrepancies in the solution are found in P1 cases. The current loop in the upper part of the plume due to the local null current condition in P1L is absent in case P1G, whose solution is significantly less affected by the plume truncation, and remains much closer to that of P2G-P4G cases. Even though the P boundary cuts the cathode magnetic line in P1 cases, the GDML model limits the influence of the plume size on the ion beam neutralization downstream, as it allows the main current loop that develops in this region to close at *infinity*, thus providing a more robust $\tilde{\jmath}$ solution against plume truncation. Therefore, the GDML model increases the reliability of the simulation results for smaller, less computationally demanding plume domains.

Figures 4(a) and 4(b) shows 2D maps of $\tilde{\jmath}_e$ magnitude and streamlines for cases P3L and P3G, respectively. Along the cathode magnetic line, the cathode-born electron streamlines split into two electron beams: one progressively moves across the magnetic field into the thruster chamber to ionize the neutral gas and sustain the discharge, and the other flows downstream to neutralize the main ion beam. The comparison of cases P3L and P3G reveals significant
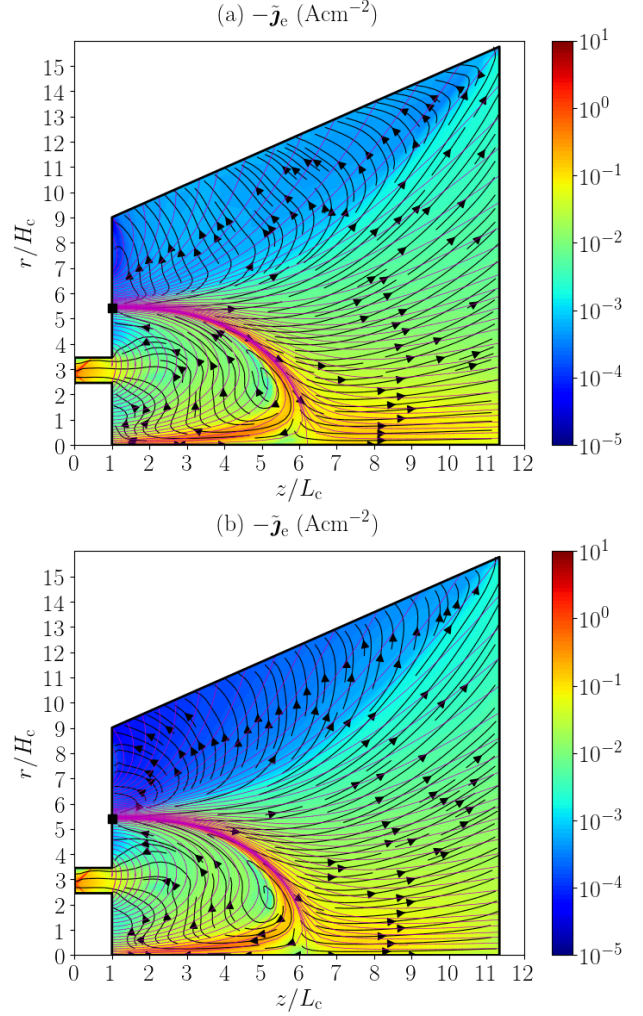

Figure 4: Time-averaged 2D (z,r) contour maps for cases P3L (a) and P3G (b) of magnitude of $\tilde{\jmath}_e$. Black lines with arrows depict the streamlines of $-\tilde{\jmath}_e$. Magenta lines indicate magnetic lines. The black square marker indicates the cathode location.

changes in this latter electron flow. In particular, in case P3L the local null current condition yields higher electron current to most of the lateral plume boundary to locally cancel the ion one there. This result is in line with the observations reported in Ref. 27, where the authors note that if the plume boundaries are set too close to the channel exit, the transport of electrons in the near plume gets perturbed by the local null current condition, and more electron current across magnetic field lines may occur. Compared to case P3L, the electron streamlines coming out the cathode in case P3G reveal a smoother transition of the electron flow towards the lateral plume boundary, following more closely the magnetic field lines there. This solution seems more representative of the still significantly magnetized electron population in the plume region simulated, where the average effective Hall parameter takes values between 65 and 245.

To complete the results described above, Fig. 5 plots relevant quantities along the P boundary for cases P3G (black solid lines) and P3L (red dashed lines). The abscissa length s runs along P from the
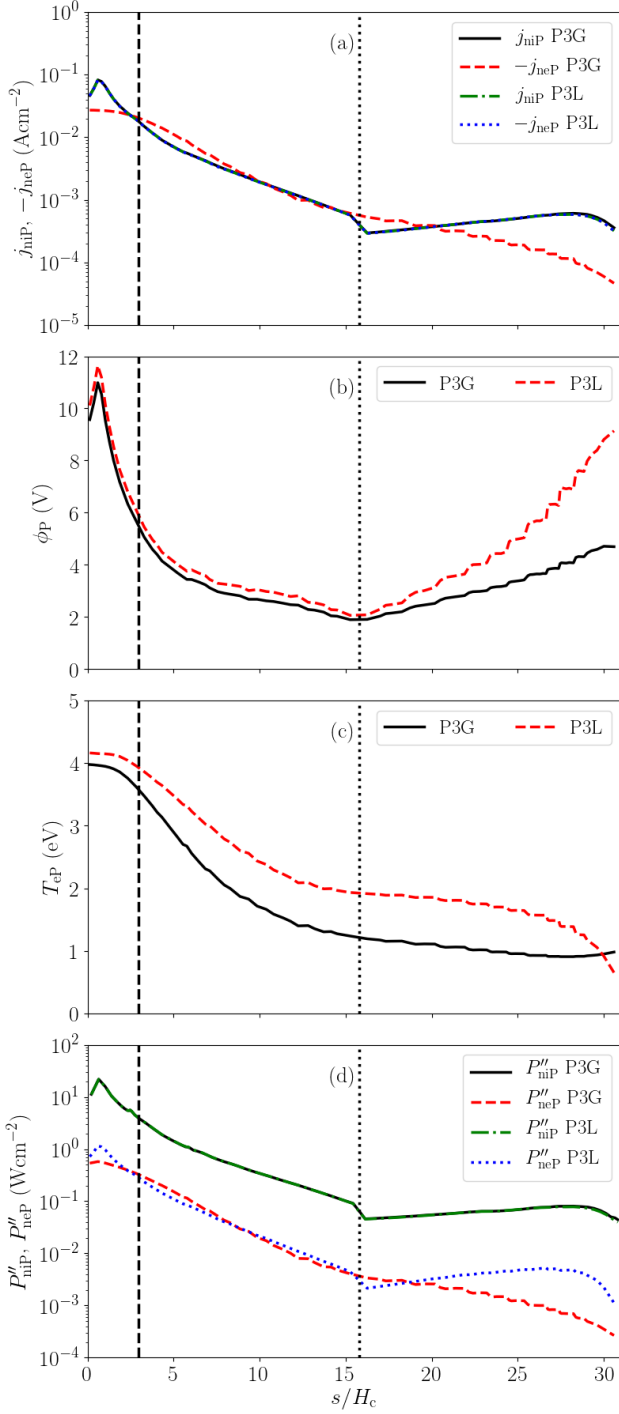
Figure 5: Time-averaged profiles along P of (a) j_{niP}, (b) $-j_{neP}$, (c) ϕ_P, (d) T_{eP}, (e) P''_{niP} and (f) P''_{neP}. Coordinate s runs along P with $s = 0$ at the symmetry axis. The vertical black dashed and dotted lines correspond to the thruster channel midradius and the upper right corner of the plume domain, respectively.

bottom right corner (i.e. at the symmetry axis) to the upper left corner of the plume domain. On each plot, the vertical black dashed line indicates the crossing point with the thruster channel midline and the vertical black dotted line indicates the location of the upper right corner of the plume domain thus separating its lateral and axial boundaries, hereafter referred to as P_{lat} and P_{ax}.

Fig. 5(a) confirms that the collected ion current profile at P is essentially the same in cases P3L and P3G so that, as discussed above, the ion expansion is practically unaffected by the electron boundary condition at P. The ion beam current leaving the simulation domain through P I_{iP} takes values around 16.7A for all cases (refer to Tab. A.1) and around a 15% of it leaves the domain through P_{lat} in both cases, being mainly carried by high-divergence fast ions and slow CEX ions generated in the core of the ion beam exiting the thruster channel. The contribution of CEX species to the ion current leaving the simulation domain through P_{lat} is about 1%.

In Fig. 5(b), local j_{neP} values for case P3G do not coincide with $-j_{niP}$ (as for case P3L), and, according to Eq. (5), are instead mainly controlled by the local ratio $e\phi_{\infty P}/T_{eP}$, which ranges around 2-8 for a globally current-free plume. For cases P1G-P4G, this ratio averaged over P changes mildly with plume size, ranging in 4.05-4.69, with an average T_{eP} between 1.26 and 1.50 eV. These values are not far from results obtained in previous kinetic studies on magnetized plumes and indicate that the total potential fall to infinity is set mainly by the electron thermal energy [30].

While in case P3L the total electron current leaving the simulation domain through P_{lat} is equal to the corresponding ion current and represents a 15% of I_{iP}, in case P3G it amounts to about 10% of I_{iP} only. The different j_{neP} distribution in cases P3L and P3G affects the electric potential profile along P, shown in Fig. 5(c), which is locally adjusted to satisfy current continuity at the MFAM boundary cells. Compared to case P3G, case P3L features higher ϕ_P values, especially along P_{lat}, where a higher P-to-cathode bias is required to extract a larger electron current, locally equal to the ion one.

Figs. 5(e) and (f) plot the profiles along P of the ion and electron energy fluxes at the quasineutral boundary P, P''_{niP} and P''_{neP}, respectively. These energy fluxes are shaped by the corresponding j_{ni} and j_{ne} profiles on each case. Values of P''_{niP} do not include the additional ion energy gain in the GDML (negligible compared to average ion energy at P) and account for all ion species simulated. They confirm that the energy content of the ion beam is not affected by the electron boundary condition at P. As expected, the ion energy flux at P is about 1-2 orders of magnitude larger than the electron one, P''_{neP}. For case P3L, $|eP''_{neP}/(j_{neP}T_{eP})| = c = 4.5$, according to Eq. (2). On the other hand, for the case P3G, P''_{neP} is given by Eq. (7), and depends on the local ratio $e\phi_{\infty P}/T_{eP}$. The resulting electron temperature along P is lower than that of case P3L along most of the downstream plume boundary, as shown in Fig. 5(b), with $|eP''_{neP}/(j_{neP}T_{eP})| \sim 3-7$.

4 Effects of cathode location on current maps and cathode coupling

Tab. 2 gathers F and its contributions for cases PiLC and PiGC, with $i = 2, 3$, with the cathode located in the external region outside the magnetic separatrix (refer to Sec. 2.3). The comparison with corresponding cases PiL and PiG, with $i = 2, 3$, analyzed in Sec. 3, with the cathode located in the internal region enclosed by the magnetic separatrix reveals the same trends for P2 and P3 cases, although larger differences between L and G cases are observed for plume size P2, as expected. In particular, external cathode cases exhibit lower F and η values. Relative decrease on F with respect to corresponding internal cathode cases is within -4.8% and -5.8%. The decrease in η in percentage points is of 3-4% among cases. Lower F values are due to the decrease in the ion contribution to thrust F_i, which are not compensated by the increase in F_e. The worse cathode-beam coupling, indicated by higher V_{cc}, which raises from $\sim$3% of V_d to values ranging from 9.5% to 17.2% of V_d, is in line with the lower F_i values obtained. There are several experimental studies reporting results aligned with the findings here. For a cathode axially aligned with the thurster axis, in Ref. 1 authors reported a F decrease with increasing radial position of the cathode, concluding that the optimum cathode position is as close to the outer magnet pole as possible. Previous works have reported an increase in V_{cc} and poorer performance when increasing the radial position of the cathode, in particular for locations outside the magnetic separatrix [8–12]. Measurements on a HET with a magnetic topology featuring no off-axis separatrix indicated that V_{cc} increased in magnitude with the radial position of the cathode when the cathode was moved across regions of high electron magnetization, where the effective Hall parameter ranged about 500 [14]. Here, the effective Hall parameter is of about 200-300 in the cathode region.

Contributions to the ion current balance in Tab. A.1, reveal that the fraction of the produced current lost into the thruster walls decreases by 2-3%. At the same time, the corresponding increase is observed on the fraction collected at the plume. This result is in line with the higher η_{cur} values found, mainly due to the lower I_d. High η_{cur} values ($\sim$0.95-0.96), increasing with the radial position of the cathode have been reported in previous experimental studies [7, 9].

Power losses to walls in Tab. A.2 are also found to decrease by 2-4%, while inelastic losses change minimally (maximum 1%). As a result, η_{ene} increases from $\sim$0.65 to $\sim$0.68-0.70. This fact is due to the higher electron power into the plume, while the ion one is found to decrease due to the poorer ion acceleration. The increase in η_{ene} is compensated mainly by a decrease in the divergence efficiency η_{div} from 0.77 to $\sim$0.68-0.70, indicating higher plume divergence, and, in second place, by a decrease in the dispersion efficiency η_{disp} from 0.79-0.80 to 0.74-0.76 (refer to Appendix A).

Fig. 6 compares axial profiles in the near plume along the thruster channel midline for $z/L_c \leqslant 3$ for the analyzed cases here. Higher ϕ and T_e values are found in the plume when the cathode is located in the external region outside the separatrix, especially for L cases, while the n_e increases slightly along the channel midline and decreases near the axis (not shown). Effects of plume size on ϕ and T_e are amplified when the cathode is placed outside the separatrix, and are notably higher on L cases compared to G ones. At the final point of the axial profiles, it is found $T_{eP} = 12.63$ and 11.34 eV for P2LC and P3LC, and $T_{eP} = 9.46$ and 9.30 eV for P2GC and P3GC, respectively. Values of $e\phi_{\infty P}/T_{eP}$ averaged over P are 4.94 and 4.92 for P2GC and P3GC, close to those obtained in P2G and P3G cases. The trends found on these properties in the near plume are well aligned with previous works. Measurements in Ref. 3 indicated that operating the thruster from a more distant cathode rather than a closer one yields higher plasma potential and electron temperature, as well as lower plasma density in the near plume. Sommerville et al. [9] showed average values of ϕ and T_e in the near field plume to increase when increasing radial position of the cathode, particularly outside the magnetic separatrix, while average n_e values remained practically unchanged or decreased slightly. The authors noticed that higher ϕ values increased ion beam divergence due to higher radial electric field. Plasma potential in the plume was also reported to increase when placing the cathode outside the separatrix in Refs. 10 and 11, the latter reporting higher divergence. For a 6 kW HET, Jameson et al. [2] compared the operation with an externally and internally-mounted (i.e. on the axis) cathode. Higher plasma potential in the plume and V_{cc} values where obtained when operating with the external cathode, and efficiency was reported to increase by 2-3% when operating with the internal cathode. Reduced V_{cc} and plume divergence was also reported in Ref. 4 for a 8 kW HET operating with an internal cathode. Full PIC simulations have captured the lower plume divergence found in experiments when operating with a centrally-mounted [39, 40].

Fig. 7 shows the 2D maps of magnitude of $\tilde{\jmath}$ (a)-(d) and $\tilde{\jmath}_e$ (e)-(h) along with their corresponding streamlines for cases P2LC and P3LC (left column), and P2GC and P3GC (right column) ($\tilde{\jmath}_i$ shows minor differences among simulated cases and has been omitted for simplicity). For the reference cases P2-P4 analyzed in Sec. 3, the cathode magnetic line is enclosed by the separatrix, thus being fully contained within the simulation domain (i.e. it is a closed line within the domain), and it is located reasonably far from the P boundary. In these scenarios, downstream the cathode magnetic line, the plume is already globally current-free, although not locally. On the contrary, when the cathode is located outside the separatrix, the current neutralization problem in the plume becomes
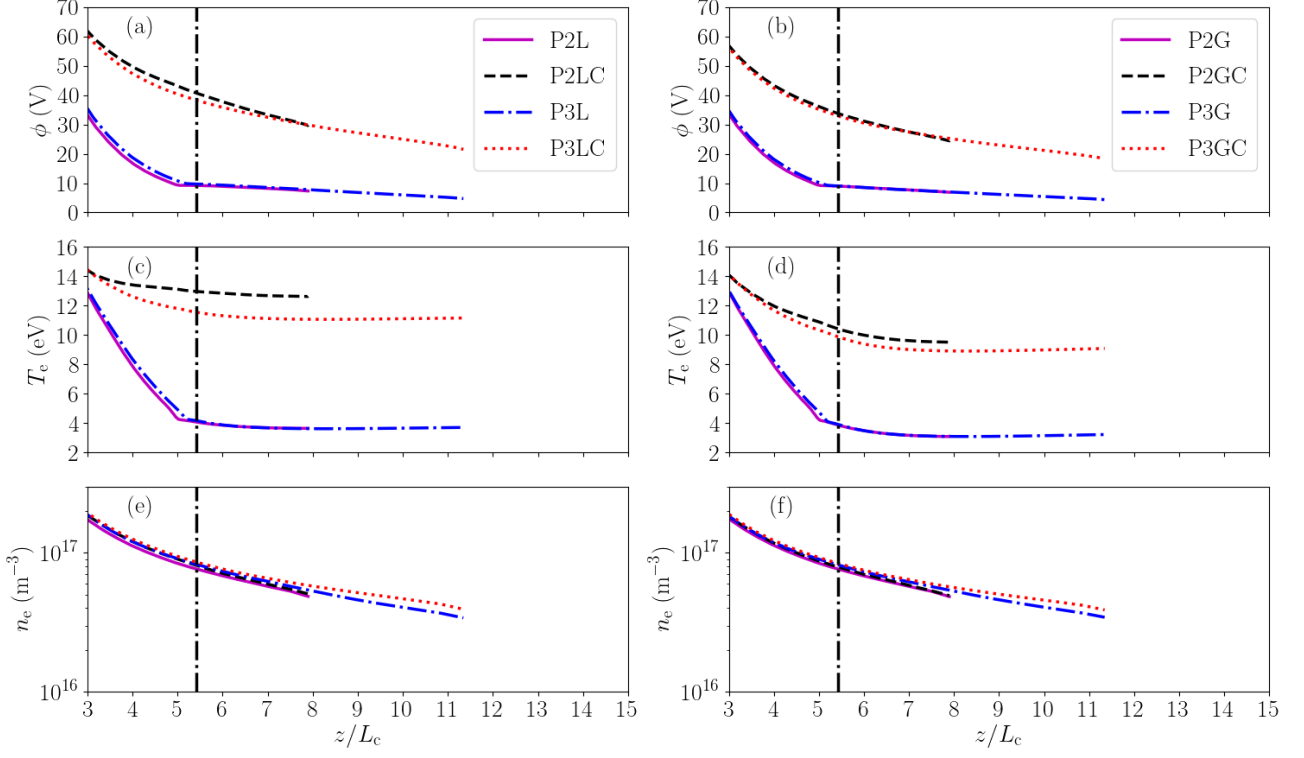
Figure 6: Time-averaged 1D axial profiles along the thruster channel midline in the near plume region for cases PiL and PiLC (left column) and cases PiG, PiGC, (right column) with $i = 2, 3$. (a)-(b) ϕ, (c)-(d) T_e and (e)-(f) n_e. The vertical black dot-dashed line indicates the crossing point with the cathode magnetic line at $z/L_c = 5.4$ for cases with the reference cathode position.

more complex and comprises a broader region in the plume since the cathode magnetic line extends downstream along the plume and crosses the P boundary. In the weakly collisional near plume plasma, a significant fraction of magnetized electrons follow near cathode field lines intersecting the P boundary, so that only there the plume becomes globally current-free. This increases the influence of the P boundary on the electric current solution. In fact, the main anode-to-cathode current loop now closes downstream the separatrix, and a secondary current loop develops above the cathode magnetic line. The performance of the local null current condition is even worse than in the reference cases analyzed in Sec. 3. It enhances plume truncation effects on these current loops by imposing $\tilde{\boldsymbol{j}}$ streamlines to be parallel to P boundary, and inducing an artificial low current region close to the axial downstream boundary, where the outer streamlines of the two current loops become tangent (the separatrix streamline departs from a $\tilde{\boldsymbol{j}} = 0$ point at P boundary). The shape, extension and location of this region notably depends on the plume size and is completely absent in G cases, for which, in contrast, these two current loops are closed within the GDML, significantly reducing plume truncation effects on the current solution.

The solution for $\tilde{\boldsymbol{j}}_e$ reveals that in the cathode near plume, cathode electrons are divided into two main beams: one travelling downstream along the cathode magnetic line, that contain only neutralizing electrons, and another along the magnetic separatrix, which distributes electrons across the magnetic field both upstream into the thruster chamber and downstream towards the P boundary. The magnetic singularity directs a large fraction of electrons from this second beam upstream into the thruster chamber (note that $-\tilde{\boldsymbol{j}}_e$ streamlines indicate the direction of the macroscopic electron flow), giving rise to a large axial electron current density at the axis upstream the magnetic singularity. Streamlines of electrons directed upstream into the thruster channel obtained from three dimensional hybrid simulations of the near plume of a HET with a similar magnetic topology revealed that, when the cathode is located at a radial position relatively far from the thruster axis, in the lateral part of the plume outside the magnetic separatrix, this electron flow was first moving from the cathode to the magnetic singular point at the thruster axis, and from there upstream into the channel [23]. Additional simulations (not shown) have revealed that, if in P2LC case the cathode is placed about 2mm farther away along the radial direction, the upstream electron flow near the axis in the region enclosed by the separatrix inverts its direction and moves downstream. This effect is induced by the local null current condition as it is not found if the GDML model is applied instead.
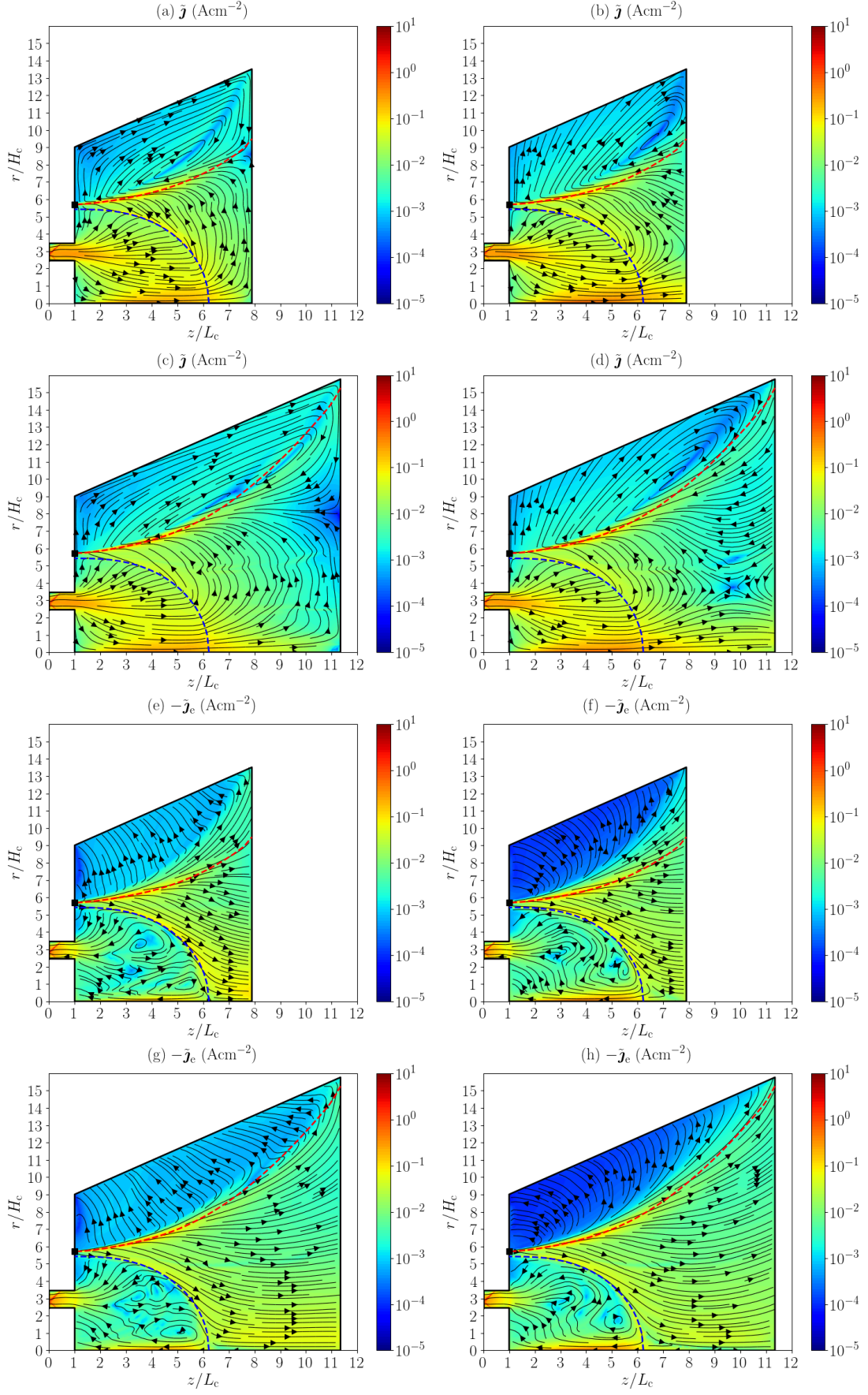
Figure 7: Time-averaged 2D (z,r) contour maps of $\tilde{\boldsymbol{\jmath}}$ (a)-(d) and $\tilde{\boldsymbol{\jmath}}_{\mathrm{e}}$ (e)-(h). Left column: P2LC and P3LC cases; right column: P2GC and P3GC cases. Rows 1 and 3 correspond to P2 cases and rows 2 and 4 to P3 cases. The black square marker indicates the cathode location. The red and blue dashed lines correspond to the cathode magnetic line and the separatrix, respectively.

5   Conclusion

The current neutralization problem in the near plume of a HET has been analyzed through HYPHEN simulations for different plume sizes and cathode locations. The local null current condition typically imposed at the plume boundary P has been compared against a newly developed GDML model, defined as a thin boundary layer that summarizes the plume expansion to infinity in the off-simulation region. The GDML model represents an improvement with respect to the local null current condition, since (1) it ensures a globally current-free plasma plume while locally decoupling ion and electron currents at P; (2) it provides expressions for the electron particle and energy fluxes at P; and (3) it permits to estimate the final electric potential in the plume.

First, placing the external cathode in the region enclosed by the magnetic separatrix, the results for four plume domain sizes have been compared with both the local null current condition and the GDML model applied at P. For all simulated cases, results reveal that the expansion of the ion beam in the near plume and the main thruster performance figures are minimally affected by the plume size and the electron outflow boundary conditions applied at P. Changes on the cathode coupling voltage and values of the final potential in the plume are small with respect to the discharge voltage. Compared to the local null current condition, the GDML model provides an electron current solution in the bulk plume domain that seems more representative of the still magnetized electron population in the near plume region, with electron streamlines following more closely the magnetic field lines there. Besides, it limits the influence of the plume boundary on the ion beam neutralization downstream providing a more robust solution for the electric current map in the near plume against the size of the near plume region simulated.

Second, when the cathode is located in the external region outside the magnetic separatrix, the GDML model clearly outperforms the local null current condition, which induces artificial low electric current regions near the plume boundary that depend on the size of the simulated plume, and that are absent when the GDML model is applied. The GDML model is shown to significantly reducing plume truncation effects on the electric current solution, thus increasing the reliability of the simulation results obtained for smaller, less computationally demanding plume domains. The trends observed on the thruster performance, and on the solution for the electric potential, the electron temperature and the plasma density in the near plume with the radial position of the cathode are in line with previous experimental and numerical results in the literature.

Future efforts will focus on evaluating the new GDML model in scenarios representative of magnetically-shielded HETs with centrally-mounted cathodes and electrodeless plasma thrusters with divergent magnetic nozzles topologies in the plume, where the electron expansion downstream extends over a broader region, and the effect of plume truncation and uncertainties on electron particle and energy fluxes are higher.

Acknowledgments

A   Current and power balances and performances

Considering all ion species simulated, the ion current balance at steady state is

$$I_{\mathrm{prod}} = I_{\mathrm{i}\infty} + I_{\mathrm{iD}} + I_{\mathrm{iA}} + I_{\mathrm{iC}}, \qquad (A.1)$$

where I_{prod} is the total ion current generated by ionization in the simulation domain; I_{iD}, I_{iA} and I_{iC} are the ion currents impacting the dielectric, anode and cathode walls, respectively; and I_{iP} is the ion beam current leaving the domain through P, which is the only one contributing to thrust. All currents are defined as positive. While I_{prod} is obtained from a volumetric integration, all the other ones are computed from particle-to-surface weighting schemes.

The propellant utilization, the current efficiency, and the charge efficiency are defined as

$$\eta_{\mathrm{u}} = \frac{\dot{m}_{\mathrm{iP}}}{\dot{m}}, \qquad \eta_{\mathrm{cur}} = \frac{I_{\mathrm{iP}}}{I_{\mathrm{d}}}, \qquad \eta_{\mathrm{ch}} = \frac{e\dot{m}_{\mathrm{iP}}}{m_{\mathrm{i}}I_{\mathrm{iP}}}, \quad (A.2)$$

respectively. Here $\dot{m} = \dot{m}_{\mathrm{A}} + \dot{m}_{\mathrm{C}}$, $\dot{m}_{\mathrm{iP}}$ is the total ion mass flow across P boundary, and $\eta_{\mathrm{ch}} = 1$ if all ions are singly charged.

Table A.1 lists I_{prod} and the fractions collected at the different boundaries for the different simulation cases. The value of I_{iC} is about one order of magnitude lower than I_{iA} for all simulation cases and has not been included.

The plasma power balance for the steady state discharge is

$$P = P_P + P_{\mathrm{D}} + P_{\mathrm{A}} + P_{\mathrm{inel}}, \qquad (A.3)$$

where: $P = I_{\mathrm{d}}V_{\mathrm{d}} + P_{\mathrm{C}}$ is the total power deposited into the plasma discharge, which is the sum of the discharge power, $P_{\mathrm{d}} = I_{\mathrm{d}}V_{\mathrm{d}}$, and the net power delivered through cathode electron emission, P_{C}, amounting to 1-2% of P; P_P is the plasma energy flow through P boundary; P_{D} and P_{A} are the power losses at the dielectric walls and at the anode wall, respectively; and P_{inel} corresponds to the power losses due to inelastic

Case	I_d (A)	I_iP (A)	I_prod (A)	$I_\mathrm{iP}/I_\mathrm{prod}$	$I_\mathrm{iD}/I_\mathrm{prod}$	$I_\mathrm{iA}/I_\mathrm{prod}$	η_u	η_cur	η_ch
P1L	18.00	16.67	23.00	0.72	0.20	0.08	0.93	0.93	0.77
P2L	18.08	16.83	23.16	0.73	0.19	0.08	0.94	0.93	0.77
P3L	17.93	16.71	22.93	0.72	0.20	0.08	0.93	0.93	0.77
P4L	17.93	16.84	23.03	0.73	0.19	0.08	0.94	0.94	0.77
P2LC	17.30	16.78	22.41	0.75	0.18	0.07	0.95	0.97	0.78
P3LC	17.20	16.82	22.40	0.75	0.18	0.07	0.95	0.98	0.78
P1G	18.00	16.74	23.06	0.73	0.19	0.08	0.93	0.93	0.77
P2G	18.07	16.79	23.10	0.73	0.20	0.07	0.93	0.93	0.77
P3G	17.90	16.79	23.05	0.73	0.19	0.08	0.93	0.94	0.77
P4G	17.90	16.75	22.90	0.73	0.19	0.08	0.93	0.94	0.77
P2GC	17.34	16.65	22.31	0.74	0.19	0.07	0.94	0.96	0.79
P3GC	17.18	16.69	22.28	0.75	0.18	0.07	0.95	0.97	0.79

Table A.1: Values of I_d, I_iP, I_prod and fractions of I_prod corresponding to the different contributions to the current balance in Eq. (A.1). Values of η_u, η_cur and η_ch, defined in Eq. (A.2).

Case	P (kW)	η	P_inel/P	P_D/P	P_A/P	P_P/P (= η_ene)	η_div	η_disp
P1L	5.47	0.39	0.08	0.20	0.06	0.66	0.76	0.78
P2L	5.50	0.40	0.09	0.20	0.06	0.65	0.77	0.79
P3L	5.45	0.40	0.09	0.20	0.06	0.65	0.77	0.80
P4L	5.45	0.41	0.09	0.20	0.06	0.65	0.78	0.80
P2LC	5.29	0.36	0.08	0.19	0.05	0.68	0.70	0.76
P3LC	5.26	0.36	0.09	0.18	0.05	0.68	0.70	0.76
P1G	5.52	0.39	0.08	0.20	0.06	0.66	0.76	0.78
P2G	5.50	0.39	0.09	0.20	0.06	0.65	0.77	0.79
P3G	5.44	0.40	0.09	0.20	0.06	0.65	0.77	0.80
P4G	5.44	0.40	0.09	0.20	0.06	0.65	0.77	0.80
P2GC	5.34	0.36	0.08	0.18	0.05	0.69	0.70	0.75
P3GC	5.31	0.36	0.09	0.17	0.05	0.69	0.70	0.75

Table A.2: Value of P and fractions of P corresponding to different contributions to the power balance in Eq. (A.3). Values of η, η_ene, η_div and η_disp, defined in Eqs. (A.4) and (A.5).

(e.g., ionization and excitation) collisions. All powers are defined as positive. The value of P_inel is obtained from a volumetric integral; P_P, is computed from the surface integral at the downstream plume boundary P (the integral of P''_niP and P''_neP yields the contribution of ions and electrons, respectively); and the values of P_D and P_A come from surface integrals at the respective walls (not at the Debye sheath edges).

The thrust efficiency is defined and factorized as

$$\eta = \frac{F^2}{2\dot m P} \equiv \eta_\mathrm{ene}\eta_\mathrm{div}\eta_\mathrm{disp}, \qquad (A.4)$$

where the energy, divergence, and dispersion efficiencies are defined, respectively, as

$$\eta_\mathrm{ene} = \frac{P_\mathrm{P}}{P} \qquad \eta_\mathrm{div} = \frac{P_\mathrm{zP}}{P_\mathrm{P}}, \qquad \eta_\mathrm{disp} = \frac{F^2}{2\dot m P_\mathrm{zP}}, \qquad (A.5)$$

with P_zP the flow of axial plasma energy across P. In Eq. (A.5), η_ene is a plasma source related efficiency that measures the relative power in the downstream plume, while plume-related efficiencies are η_div, which assesses the plume divergence based on axial energy

and total energy flows, and η_disp, that quantifies the level of velocity dispersion of all plasma species (which would be one for a mono-velocity gas).

Table A.2 lists the contributions to the power balance in Eq. (A.3) and the values of the efficiencies in Eqs. (A.4) and (A.5).

References

[1] Tilley, D., de Grys, K., and Myers, R., "Hall thruster-cathode coupling," *35th Joint Propulsion Conference and Exhibit*, 1999, p. 2865.

[2] Jameson, K. K., Goebel, D. M., Hofer, R. R., and Watkins, R. M., "Cathode coupling in Hall thrusters," 30th *International Electric Propulsion Conference*, No. IEPC-2007-278, Electric Rocket Propulsion Society, Fairview Park, OH, Florence, Italy, September 17–20, 2007.

[3] Beal, B. E., Gallimore, A. D., and Hargus Jr, W. A., "Effects of cathode configuration on Hall thruster cluster plume properties," *Journal of*

Propulsion and Power, Vol. 23, No. 4, 2007, pp. 836–844.

[4] Hofer, R., Johnson, L., Goebel, D., and Wirz, R., "Effects of internally mounted cathodes on Hall thruster plume properties," *IEEE Transactions on Plasma Science*, Vol. 36, No. 5, 2008, pp. 2004–2014.

[5] McDonald, M. and Gallimore, A., "Cathode position and orientation effects on cathode coupling in a 6-kW Hall thruster," 31st *International Electric Propulsion Conference*, No. IEPC-2009-113, Electric Rocket Propulsion Society, Fairview Park, OH, University of Michigan, Ann Arbor, MI, USA, September 20-24, 2009.

[6] Sommerville, J. and King, L., "Effect of cathode position on Hall-effect thruster performance and cathode coupling voltage," 30th *International Electric Propulsion Conference*, No. IEPC-2007-78, Electric Rocket Propulsion Society, Fairview Park, OH, Florence, Italy, September 17-20, 2007.

[7] Sommerville, J. and King, L., "Effect of cathode position on Hall-effect thruster performance and near-field plume properties," *44th AIAA/ASME/SAE/ASEE Joint Propulsion Conference & Exhibit*, No. AIAA-2008-4996, American Institute of Aeronautics and Astronautics, Reston, VA, Hartford, CT, USA, July 21-23, 2007.

[8] Sommerville, J. D. and King, L. B., "Hall-effect thruster–cathode coupling, part I: efficiency improvements from an extended outer pole," *Journal of Propulsion and Power*, Vol. 27, No. 4, 2011, pp. 744–753.

[9] Sommerville, J. D. and King, L. B., "Hall-effect thruster–cathode coupling, part II: ion beam and near-field plume," *Journal of Propulsion and Power*, Vol. 27, No. 4, 2011, pp. 754–767.

[10] Turan, N., Kokal, U., Celik, M., and Kurt, H., "Experimental study of the effects of the cathode position and the electrical circuit configuration on the operation of HK40 Hall thruster and BUSTLab hollow cathode," *52nd AIAA/SAE/ASEE Joint Propulsion Conference*, No. AIAA-2016-4834, American Institute of Aeronautics and Astronautics, Reston, VA, Salt Lake City, UT, USA, July 25-27, 2016.

[11] Yu, D., Meng, T., Ning, Z., and Liu, H., "Confinement effect of cylindrical-separatrix-type magnetic field on the plume of magnetic focusing type Hall thruster," *Plasma Sources Science and Technology*, Vol. 26, No. 4, 2017, pp. 04LT02.

[12] Ding, Y., Li, H., Li, P., Jia, B., Wei, L., Su, H., Sun, H., Wang, L., and Yu, D., "Effect of relative position between cathode and magnetic separatrix on the discharge characteristic of Hall thrusters," *Vacuum*, Vol. 154, 2018, pp. 167–173.

[13] Frieman, J. D., King, S. T., Walker, M. L., Khayms, V., and King, D., "Role of a conducting vacuum chamber in the Hall effect thruster electrical circuit," *Journal of Propulsion and Power*, Vol. 30, No. 6, 2014, pp. 1471–1479.

[14] Frieman, J. D., Walker, J. A., Walker, M. L., Khayms, V., and King, D. Q., "Electrical facility effects on Hall thruster cathode coupling: Performance and plume properties," *Journal of Propulsion and Power*, Vol. 32, No. 1, 2016, pp. 251–264.

[15] Walker, J. A., Frieman, J. D., Walker, M. L., Khayms, V., King, D., and Peterson, P. Y., "Electrical facility effects on Hall-effect-thruster cathode coupling: discharge oscillations and facility coupling," *Journal of Propulsion and Power*, Vol. 32, No. 4, 2016, pp. 844–855.

[16] Walker, J. A., Langendorf, S. J., Walker, M. L., Khayms, V., King, D., and Pertson, P., "Electrical facility effects on Hall current thrusters: electron termination pathway manipulation," *Journal of Propulsion and Power*, Vol. 32, No. 6, 2016, pp. 1365–1377.

[17] Fife, J. M., *Hybrid-PIC modeling and electrostatic probe survey of Hall thrusters*, Ph.D. thesis, Massachusetts Institute of Technology, 1998.

[18] Hagelaar, G., Bareilles, J., Garrigues, L., and Boeuf, J., "Two-dimensional model of a stationary plasma thruster," *Journal of Applied Physics*, Vol. 91, No. 9, 2002, pp. 5592–5598.

[19] Parra, F. I., Ahedo, E., Fife, J. M., and Martínez-Sánchez, M., "A two-dimensional hybrid model of the Hall thruster discharge," *Journal of Applied Physics*, Vol. 100, No. 2, 2006, pp. 023304.

[20] Garrigues, L., Hagelaar, G., Boniface, C., and Boeuf, J., "Anomalous conductivity and secondary electron emission in Hall effect thrusters," *Journal of applied physics*, Vol. 100, No. 12, 2006, pp. 123301.

[21] Sommier, E., Scharfe, M., Gascon, N., Cappelli, M., and Fernandez, E., "Simulating plasma-induced Hall thruster wall erosion with a two-dimensional hybrid model," *Plasma Science, IEEE Transactions on*, Vol. 35, No. 5, 2007, pp. 1379–1387.

[22] Perales-Díaz, J., Domínguez-Vázquez, A., Fajardo, P., Ahedo, E., Faraji, F., Reza, M., and Andreussi, T., "Hybrid plasma simulations of a magnetically shielded Hall thruster," *Journal of Applied Physics*, Vol. 131, No. 10, 2022, pp. 103302.

[23] Cichocki, F., Domínguez-Vázquez, A., Merino, M., Fajardo, P., and Ahedo, E., "Three-dimensional neutralizer effects on a Hall-effect thruster near plume," *Acta Astronautica*, Vol. 187, 2021, pp. 498–510.

[24] Mikellides, I. and Katz, I., "Numerical simulations of Hall-effect plasma accelerators on a magnetic-field-aligned mesh," *Physical Review E*, Vol. 86, No. 4, 2012, pp. 046703.

[25] Keidar, M., Boyd, I. D., and Beilis, I. I., "Modeling of a high-power thruster with anode layer," *Physics of Plasmas*, Vol. 11, No. 4, 2004, pp. 1715–1722.

[26] Andreussi, T., Giannetti, V., Leporini, A., Saravia, M. M., and Andrenucci, M., "Influence of the magnetic field configuration on the plasma flow in Hall thrusters," *Plasma Phys. Control. Fusion*, Vol. 60, No. 1, 2018.

[27] Lopez Ortega, A. and Mikellides, I. G., "The importance of the cathode plume and its interactions with the ion beam in numerical simulations of Hall thrusters," *Physics of Plasmas*, Vol. 23, No. 4, 2016, pp. 043515.

[28] Mikellides, I. G., Katz, I., Hofer, R. R., and Goebel, D. M., "Hall-effect thruster simulations with 2-D electron transport and hydrodynamic ions," *31st International Electric Propulsion Conference*, paper 2009-114, Electric Rocket Propulsion Society, Fairview Park, OH, University of Michigan, Ann Arbor, MI, USA, 2009.

[29] Kubota, K., Cho, S., Watanabe, H., and Funaki, I., "Hybrid-PIC Simulation of Hall Thruster with Internally Mounted Cathode," *35th International Electric Propulsion Conference*, IEPC-2017-426, Atlanta, GA, USA, 2017.

[30] Ahedo, E., Correyero, S., Navarro, J., and Merino, M., "Macroscopic and parametric study of a kinetic plasma expansion in a paraxial magnetic nozzle," *Plasma Sources Science and Technology*, Vol. 29, No. 4, 2020, pp. 045017.

[31] Merino, M., Mauriño, J., and Ahedo, E., "Kinetic electron model for plasma thruster plumes," *Plasma Sources Science and Technology*, Vol. 27, No. 3, 2018, pp. 035013.

[32] Li, M., Merino, M., Ahedo, E., and Tang, H., "On electron boundary conditions in PIC plasma thruster plume simulations," *Plasma Sources Science and Technology*, Vol. 28, No. 03, 2019, pp. 034004.

[33] Domínguez-Vázquez, A., *Axisymmetric simulation codes for Hall effect thrusters and plasma plumes*, Ph.D. thesis, Universidad Carlos III de Madrid, Leganés, Spain, 2019.

[34] Domínguez-Vázquez, A., Zhou, J., Fajardo, P., and Ahedo, E., "Analysis of the plasma discharge in a Hall thruster via a hybrid 2D code," 36th *International Electric Propulsion Conference*, No. IEPC-2019-579, Electric Rocket Propulsion Society, Vienna, Austria, 2019.

[35] Zhou, J., *Modeling and simulation of the plasma discharge in a radiofrequency thruster*, Ph.D. thesis, Universidad Carlos III de Madrid, Leganés, Spain, 2021.

[36] Zhou, J., Domínguez-Vázquez, A., Fajardo, P., and Ahedo, E., "Magnetized fluid electron model within a two-dimensional hybrid simulation code for electrodeless plasma thrusters," *Plasma Sources Science and Technology*, Vol. 31, No. 4, 2022, pp. 045021.

[37] Pérez-Grande, D., González-Martínez, O., Fajardo, P., and Ahedo, E., "Analysis of the numerical diffusion in anisotropic mediums: benchmarks for magnetic field aligned meshes in space propulsion simulations," *Applied Sciences*, Vol. 6, No. 11, 2016, pp. 354.

[38] Jorns, B. A. and Byrne, M. P., "Model for the dependence of cathode voltage in a Hall thruster on facility pressure," *Plasma Sources Science and Technology*, Vol. 30, No. 1, 2021, pp. 18.

[39] Cho, S., Kubota, K., Watanabe, H., Hara, K., and Funaki, I., "Comparing Internal and External Cathode Boundary Position in a Hall Thruster Particle Simulation," 35th *International Electric Propulsion Conference*, No. IEPC-2017-402, Electric Rocket Propulsion Society, Fairview Park, OH, Georgia Institute of Technology, Atlanta, GA, USA, October 8-12, 2017.

[40] Cao, X., Liu, H., and Yu, D., "Simulation of discharge process of Hall thruster under the internal and external cathode conditions," *The European Physical Journal Applied Physics*, Vol. 90, No. 1, 2020, pp. 10801.